Journal of Computational Physics 228 (2009) 8283–8300

Contents lists available at ScienceDirect

Journal of Computational Physics

journal homepage: www.elsevier.com/locate/jcp

High order conservative differencing for viscous terms and the application to vortex-induced vibration flows

Yiqing Shen, Gecheng Zha *, Xiangying Chen

Dept. of Mechanical and Aerospace Engineering, Miami Wind™, University of Miami, Coral Gables, FL 33124, United States

ARTICLE INFO

Article history:
Received 12 January 2009
Received in revised form 31 July 2009
Accepted 9 August 2009
Available online 18 August 2009

Keywords:
Central differencing
High order accuracy
Navier–Stokes equations
Viscous terms
Vortex-induced vibration

ABSTRACT

A new set of conservative 4th-order central finite differencing schemes for all the viscous terms of compressible Navier–Stokes equations are proposed and proved in this paper. These schemes are used with a 5th-order WENO scheme for inviscid flux and the stencil width of the central differencing scheme is designed to be within that of the WENO scheme. The central differencing schemes achieve the maximum order of accuracy in the stencil. This feature is important to keep the compactness of the overall discretization schemes and facilitate the boundary condition treatment. The algorithm is used to simulate the vortex-induced oscillations of an elastically mounted circular cylinder. The numerical results agree favorably with the experiment.

1. Introduction

High order (higher than 2nd-order) finite differencing algorithms have attracted more and more interest recently due to the increased demand to accurately predict engineering problems and understand fundamental flow physics [1,2]. For example, the direct numerical simulation (DNS) of turbulence and aeroacoustics requires high order discretization schemes with low diffusion to resolve different scale turbulence eddies and acoustic propagation. Fluid–structure interaction simulation also requires low numerical dissipation in order to accurately predict flow damping and structure response.

High order accuracy requires high order evaluation of both the inviscid and viscous fluxes. However, most of research focus on the inviscid fluxes to resolve discontinuities. For example, the essentially non-oscillatory (ENO) schemes [3,4] and weighted essentially non-oscillatory (WENO) schemes [5–9] are all aimed at resolving the inviscid fluxes with high order accuracy in smooth regions and achieving the capability to capture shock wave and contact discontinuities.

To capture discontinuities, the hyperbolic equations need to be solved in a conservative manner. A conservative numerical discretization is also essential to satisfy the conservation laws of fluid physics. A finite volume method based on the integral form of Navier–Stokes equations has the advantage to naturally obtain flux conservation. For finite differencing method, a partial derivative needs to be discretized using the interface location between two solution points in order to be conservative.

For example, the following is a conservative finite differencing scheme.

$$\frac{\partial f}{\partial x_i} = \frac{f_{i+1/2} - f_{i-1/2}}{\Delta x} \tag{1}$$

* Corresponding author. Tel.: +1 3052843328.
E-mail addresses: yqshen@miami.edu (Y. Shen), gzha@miami.edu (G. Zha).

0021-9991/$ - see front matter © 2009 Elsevier Inc. All rights reserved.
doi:10.1016/j.jcp.2009.08.004

If the function $f_{i+1/2}$ is reconstructed with higher than 2nd-order accuracy, Eq. (1) will give at least a 2nd-order accuracy conservative scheme.

For 2nd-order accuracy schemes, there is not much difference for the computational amount between a finite volume or finite differencing scheme. However, for high order WENO schemes, it is very different. As pointed out by Titarev et al. and Zhou et al. [10,11], when the piece-wise parabolic reconstruction is used in two space dimensions, a finite volume WENO scheme requires approximately three times more CPU time than the corresponding finite difference WENO scheme. In three space dimensions, the difference is about nine times. Hence, for structured meshes, finite difference WENO schemes are preferred. For the inviscid fluxes, finite difference WENO schemes only need to handle first order derivatives. The WENO reconstruction is designed to ensure a conservative discretization of the first order derivatives [5–9].

To discretize the viscous terms using finite differencing schemes, it is important that the stencil width of the viscous term discretization does not exceed the WENO stencil width. Otherwise, the overall stencil width will be wider than the WENO stencil and the advantage of the WENO scheme achieving a certain high order scheme within a compact stencil is lost. In addition, the narrower the stencil, the easier to treat boundary conditions.

The design of the central differencing schemes for the viscous terms in this paper hence is required to satisfy the following three constraints: (1) achieve minimum 4th order accuracy; (2) be conservative; and (3) the stencil width must be less than that of the 5th-order WENO scheme. To satisfy these constraints, it is realized that the finite differencing has to achieve the maximum order of accuracy within the WENO stencil.

However, for the viscous fluxes that contain 2nd-order derivatives, such as

$$\frac{\partial}{\partial x}\left(\mu\frac{\partial f}{\partial x}\right) \quad \text{or} \quad \frac{\partial}{\partial x}\left(\mu\frac{\partial f}{\partial y}\right), \tag{2}$$

where μ is the viscosity coefficient, achieving a finite differencing scheme with both high order accuracy and flux conservation is not trivial. Usually, a 2nd-order derivative is discretized first by a high order differencing of the first order derivative, and then the same differencing scheme is applied again to obtain high order discretization of the 2nd-order derivative. These methods include the standard high order finite differencing schemes directly discretized on the node points as well as the compact central differencing schemes [12].

If the viscosity coefficient is constant, the conservative high order schemes are straightforward, for example, a 4th-order discretization can be constructed by using five points. However, if the viscosity coefficient is variable as in compressible flows, the conservative high order finite differencing schemes for those viscous terms are not obvious. A conservative finite differencing scheme for the cross derivatives are even more complicated.

If a standard central difference scheme is used, the discretization for a 2nd-order derivative will involve a large number of grid points with a wide stencil. For example, for 4th-order accuracy, the following discretization will have

$$\left.\frac{\partial}{\partial x}\left(\mu\frac{\partial f}{\partial x}\right)\right|_i = \frac{1}{\Delta x}\sum_{k=-2}^{k=2}\beta_k\mu_{i+k}\left.\frac{\partial f}{\partial x}\right|_{i+k} + O(\Delta x^4) \tag{3}$$

and

$$\left.\frac{\partial f}{\partial x}\right|_l = \frac{1}{\Delta x}\sum_{k=-2}^{k=2}\beta_k f_{l+k} + O(\Delta x^4) \tag{4}$$

where β_k are the coefficients to make Eqs. (3) and (4) achieve 4th-order accuracy. The stencil width of the viscous term discretization in Eq. (3) is hence $(f_{i+4}, f_{i+3}, \ldots, f_{i-4})$ and is greater than that of the 5th-order WENO scheme $(f_{i+3}, f_{i+2}, \ldots, f_{i-3})$.

De Rango and Zingg [13] and Zingg et al. [14] suggested a 4th-order accuracy conservative scheme for the viscous terms. However, their schemes do not achieve the maximum order accuracy within the stencil width used. In addition, they do not have conservative finite differencing schemes to treat the 2nd-order cross derivatives.

The purpose of this paper is to develop a set of reconstruction formula to achieve conservative 4th-order accuracy central differencing schemes for all the 2nd-order derivative viscous terms of compressible Navier–Stokes equations in generalized coordinates. Such conservative schemes are essential to be used with the conservative 5th-order WENO schemes to enhance the overall accuracy of the flow solutions. The 4th order schemes studied in this paper were first presented in [15]. This paper gives the proof.

The other special numerical technique used in this paper is that the solution points are not located at the grid nodes as a standard finite differencing method. Instead, they are shifted by half a grid interval from the grid nodes in every direction in the generalized computation domain. In this way, they are exactly located at the centroid of a grid cell in the generalized coordinates. In physical domain, they may not be in the centroid of a cell. There are two very useful advantages of this treatment: (1) it is straightforward to impose accurate boundary conditions such as no slip conditions; and (2) the grid cell interfaces are the location to evaluate the conservative flux or derivative reconstruction. It hence allows a direct use of the computer code structure of a low order finite volume code with the solution points located in the centroids of grid cells.

1.1. Application to vortex-induced vibration flows

The practical significance of vortex-induced vibrations of basic fluid dynamics and engineering applications has led to a large number of experimental and numerical investigations. Sarpkaya [16] and Williamson and Govardhan [17,18] gave

comprehensive overviews on the vortex-induced vibration flows (VIV). Al Jamal and Dalton [19] reviewed recent numerical studies on VIV of a circular cylinder and investigated the irregular behavior of the phase angle. An overview is also given for the numerical methods used in solving the fully coupled fluid–structure interaction problem by Gabbai and Benaroya [20].

Various CFD methods are employed to study vortex-induced vibration flows, including the Reynolds Averaged Navier–Stokes (RANS) methods, Large Eddy Simulations (LES), Direct Numerical Simulations (DNS), and their various combinations. DNS are usually restricted to low Reynolds number flows. LES has been used to solve the problem at moderate Reynolds numbers. Meynen et al. [21] used a 2nd-order finite volume method with a central differencing scheme and the Crank–Nicholson scheme. Mittal and Kumar [22–24] used the space-time finite element approach. Blackburn et al. [25,26] utilized a spectral element-Fourier spatial discretion method to solve the incompressible NS equations. DNS based on spectral element methods are employed in Refs. [27–29]. The Beam-Warming central difference scheme is employed to solve the compressible NS equations in [30]. A spectral-element method [31] and second-order Monotone Advection and Reconstruction Scheme [32] were employed to solve incompressible Navier–Stokes equations. The second-order consistent physical interpolation approach is used to solve the 2D unsteady Navier–Stokes equations by Guilmineau and Queutey [33,34] and the third-order upwind difference scheme QUICK is applied to solve the SST $k-\epsilon$ turbulence model by Pan et al. [35]. The LES is also carried out by using a finite element method [36] and the standard second-order finite difference scheme [19,37]. Chen and Zha [38,39] developed a fully coupled fluid-structural interaction method, in which the 3rd order MUSCL differencing for inviscid fluxes and 2nd-order central differencing for viscous terms are used. Except the spectral methods, the finite differencing schemes in the aforementioned research work are all at 2nd-order accuracy.

In this paper, a 5th-order accuracy WENO scheme for the inviscid fluxes and the new 4th order conservative central differencing for the viscous terms are used to simulate the cylinder flows due to vortex-induced cylinder vibration. Since there are no shock discontinuities in the cylinder flows, the WENO scheme is fixed to its optimal weights to achieve minimum dissipation. The fully coupled fluid-structural interaction strategy developed by Chen and Zha [38,39] is employed.

2. Numerical methods

2.1. Flow governing equations

The normalized Navier–Stokes equations governing compressible viscous flows can be written in the Cartesian coordinate as:

$$\frac{\partial Q}{\partial t}+\frac{\partial E}{\partial x}+\frac{\partial F}{\partial y}+\frac{\partial G}{\partial z}=\frac{1}{Re}\left(\frac{\partial R}{\partial x}+\frac{\partial S}{\partial y}+\frac{\partial T}{\partial z}\right) \tag{5}$$

$$Q=\begin{bmatrix}\rho\\ \rho u\\ \rho v\\ \rho w\\ \rho e\end{bmatrix},\quad E=\begin{bmatrix}\rho u\\ \rho u^2+p\\ \rho uv\\ \rho uw\\ (\rho e+p)u\end{bmatrix},\quad F=\begin{bmatrix}\rho v\\ \rho uv\\ \rho v^2+p\\ \rho vw\\ (\rho e+p)v\end{bmatrix},\quad G=\begin{bmatrix}\rho w\\ \rho uw\\ \rho vw\\ \rho w^2+p\\ (\rho e+p)w\end{bmatrix},$$

$$R=\begin{bmatrix}0\\ \tau_{xx}\\ \tau_{xy}\\ \tau_{xz}\\ u_k\tau_{xk}-q_x\end{bmatrix},\quad S=\begin{bmatrix}0\\ \tau_{xy}\\ \tau_{yy}\\ \tau_{yz}\\ u_k\tau_{yk}-q_y\end{bmatrix},\quad T=\begin{bmatrix}0\\ \tau_{xz}\\ \tau_{yz}\\ \tau_{zz}\\ u_k\tau_{zk}-q_z\end{bmatrix},$$

The repeated index k stands for the Einstein summation over x, y and z. The stress τ and heat flux q are,

$$\tau_{ik}=\mu\left[\left(\frac{\partial u_i}{\partial x_k}+\frac{\partial u_k}{\partial x_i}\right)-\frac{2}{3}\delta_{ik}\frac{\partial u_j}{\partial x_j}\right]$$

$$q_j=\frac{-\mu}{(\gamma-1)M_\infty^2 Pr}\frac{\partial T}{\partial x_j}$$

The equation of state is

$$\rho e=\frac{p}{\gamma-1}+\frac{1}{2}\rho(u^2+v^2+w^2)$$

In the above equations, ρ is the density, u, v, and w are the Cartesian velocity components in x, y and z directions, p is the static pressure, and e is the total energy per unit mass, μ is the molecular viscosity, γ, Re, M_∞ and Pr are the ratio of specific heat, Reynolds number, Mach number and Prandtl number, respectively.

In the generalized coordinates, Eq. (5) can be written as:

$$\frac{\partial Q'}{\partial t}+\frac{\partial E'}{\partial \xi}+\frac{\partial F'}{\partial \eta}+\frac{\partial G'}{\partial \zeta}=\frac{1}{Re}\left(\frac{\partial R'}{\partial \xi}+\frac{\partial S}{\partial \eta}+\frac{\partial T'}{\partial \zeta}\right) \tag{6}$$

where

$$\begin{aligned}
Q' &= \frac{1}{J}Q \\
E' &= \frac{1}{J}(\xi_t U+\xi_x E+\xi_y F+\xi_z G) \\
F' &= \frac{1}{J}(\eta_t U+\eta_x E+\eta_y F+\eta_z G) \\
G' &= \frac{1}{J}(\zeta_t U+\zeta_x E+\zeta_y F+\zeta_z G) \\
R' &= \frac{1}{J}(\xi_x R+\xi_y S+\xi_z T) \\
S' &= \frac{1}{J}(\eta_x R+\eta_y S+\eta_z T) \\
T' &= \frac{1}{J}(\zeta_x R+\zeta_y S+\zeta_z T)
\end{aligned}$$

For simplicity, the prime $'$ in Eq. (6) will be omitted. In above equations, J is the transformation Jacobian.

It was pointed out by Thomas and Lombard [40] that, due to the mixed temporal and spatial derivatives after discretization, an additional term appears, which theoretically equals zero, but numerically still remains. Consequently, numerical error could be introduced in the discretized form of the equations of the flow motion if this term is neglected. In order to reduce or avoid this error, the geometric conservation law(GCL) needs to be enforced.

There are various ways in which the GCL may be satisfied [41]. One approach is to add the following additional term to the right-hand side of the equations as a source term of the governing Eq. (6):

$$\mathbf{S}=\mathbf{Q}'\left[\frac{\partial J^{-1}}{\partial t}+\left(\frac{\xi_t}{J}\right)_{\xi}+\left(\frac{\eta_t}{J}\right)_{\eta}+\left(\frac{\zeta_t}{J}\right)_{\zeta}\right] \tag{7}$$

Another approach consists of rewriting the governing Eq. (6) as

$$\frac{\partial Q}{\partial t}=-J\left(\frac{\partial E'}{\partial \xi}+\frac{\partial F'}{\partial \eta}+\frac{\partial G'}{\partial \zeta}-\frac{1}{Re}\left[\frac{\partial R'}{\partial \xi}+\frac{\partial S'}{\partial \eta}+\frac{\partial T'}{\partial \zeta}\right]+Q(1/J)_t\right) \tag{8}$$

and then evaluate $(1/J)_t$ by using the GCL identity, i.e.,

$$\frac{\partial J^{-1}}{\partial t}=-\left[\left(\frac{\xi_t}{J}\right)_{\xi}+\left(\frac{\eta_t}{J}\right)_{\eta}+\left(\frac{\zeta_t}{J}\right)_{\zeta}\right] \tag{9}$$

There are various methods for solving (9) (see [41–44]).

In this paper, the first approach is used.

2.2. The 5th-order WENO Scheme [5]

The finite difference 5th-order accuracy WENO scheme suggested by Jiang and Shu [5] is used for the inviscid flux. The 5th-order accurate WENO ($r=3$) reconstruction of u^L can be written as

$$u^L_{i+1/2}=\omega_0 q_0+\omega_1 q_1+\omega_2 q_2$$

where

$$\begin{aligned}
q_0 &= \frac{1}{3}u_{i-2}-\frac{7}{6}u_{i-1}+\frac{11}{6}u_i \\
q_1 &= -\frac{1}{6}u_{i-1}+\frac{5}{6}u_i+\frac{1}{3}u_{i+1} \\
q_2 &= \frac{1}{3}u_i+\frac{5}{6}u_{i+1}-\frac{1}{6}u_{i+2}
\end{aligned}$$

and

$$\omega_k = \frac{\alpha_k}{\alpha_0 + \cdots + \alpha_{r-1}},$$
$$\alpha_k = \frac{C_k}{(\varepsilon + IS_k)^2}, \quad k = 0, \ldots, r-1$$
$$C_0 = 0.1, \quad C_1 = 0.6, \quad C_2 = 0.3$$
$$IS_0 = \frac{13}{12}(u_{i-2} - 2u_{i-1} + u_i)^2 + \frac{1}{4}(u_{i-2} - 4u_{i-1} + 3u_i)^2$$
$$IS_1 = \frac{13}{12}(u_{i-1} - 2u_i + u_{i+1})^2 + \frac{1}{4}(u_{i-1} - u_{i+1})^2$$
$$IS_2 = \frac{13}{12}(u_i - 2u_{i+1} + u_{i+2})^2 + \frac{1}{4}(3u_i - 4u_{i+1} + u_{i+2})^2$$

where ε is introduced to avoid the denominator becoming zero. In the practical applications, ε plays an important role on the convergence, stability and accuracy of WENO scheme [15,9]. The higher the ε value, the closer the weights approaching the optimum value C_k, and hence the lower the numerical dissipation. However, when there is a shock in the flow, the ε value cannot be too large to maintain the sensitivity to the shock. In [9], $\varepsilon = 10^{-2}$ is recommended for the transonic flows with shock waves. In this paper, since there is no shock wave in the flow, we use the fixed weights $\omega_k = C_k$ to have minimum numerical dissipation.

The u^R is constructed symmetrically as u^L about $i + 1/2$.

2.3. The new 4th-order central differencing for viscous terms [15]

A set of conservative 4th-order accurate finite central differencing schemes for the viscous terms is suggested below. These central differencing schemes are constructed so that the stencil widths are within the WENO scheme stencil. This would be satisfied if the central differencing achieves their maximum order accuracy in the WENO stencil. We take the viscous flux derivative in ξ-direction as the example to explain how the schemes are constructed.

To conservatively discretize the viscous derivative term in Navier–Stokes equations Eq. (6), we have

$$\left.\frac{\partial R}{\partial \xi}\right|_i = \frac{\widetilde{R}_{i+1/2} - \widetilde{R}_{i-1/2}}{\Delta\xi} \tag{10}$$

To obtain 4th-order accuracy, $\widetilde{R}$ needs to be reconstructed as

$$\widetilde{R}_{i-1/2} = \sum_{I=i-3/2}^{i+1/2} \alpha_I R_I \tag{11}$$

where

$$\alpha_{i-3/2} = -\frac{1}{24}, \quad \alpha_{i-1/2} = \frac{26}{24}, \quad \alpha_{i+1/2} = -\frac{1}{24} \tag{12}$$

$$R_I = [(\xi_x \tau_{xx}) + (\eta_y \tau_{xy}) + (\zeta_z \tau_{xz})]_I$$
$$(\tau_{xx}) = \mu\left\{\frac{4}{3}\left[\left(\xi_x\frac{\partial u}{\partial \xi}\right) + \left(\eta_x\frac{\partial u}{\partial \eta}\right) + \left(\zeta_x\frac{\partial u}{\partial \zeta}\right)\right] - \frac{2}{3}\left[\left(\xi_y\frac{\partial v}{\partial \xi}\right) + \left(\eta_y\frac{\partial v}{\partial \eta}\right) + \left(\zeta_y\frac{\partial v}{\partial \zeta}\right)\left(\xi_z\frac{\partial w}{\partial \xi}\right) + \left(\eta_z\frac{\partial w}{\partial \eta}\right) + \left(\zeta_z\frac{\partial w}{\partial \zeta}\right)\right]\right\} \tag{13}$$

If R in Eq. (11) can be approximated with the accuracy order not lower than 4th-order, the Taylor series expansion analysis of (10) and (11) will give

$$\frac{1}{\Delta\xi}(\widetilde{R}_{i+1/2} - \widetilde{R}_{i-1/2}) = R'(\xi_i) + O(\Delta\xi^4) \tag{14}$$

and the 4th-order accuracy is achieved (to be proved later). It needs to point out that in Eq. (10), $\widetilde{R}_{i-1/2}$ cannot be replaced by $R_{i-1/2}$. Otherwise, the 4th-order accuracy cannot be achieved even though the high order approximation of $R_{i-1/2}$ is used. The 4th-order accuracy from Eqs. (10)–(14) is also based on the condition of uniform spacing $\Delta\xi = C$, which is ensured in the generalized coordinates with $\Delta\xi = \Delta\eta = \Delta\zeta = 1$.

In order to achieve the highest order accuracy of R_I with $I = i - 3/2, i - 1/2, i + 1/2$, the approximation of each term in Eq. (11) using the same stencil is given below:

$$\mu_I = \sum_{l=m}^{n} C_l^I \mu_{i+l} \tag{15}$$
$$\left.\frac{\partial u}{\partial \xi}\right|_I = \frac{1}{\Delta\xi}\sum_{l=r}^{s} D_l^I u_{i+l} \tag{16}$$
$$\left.\frac{\partial u}{\partial \eta}\right|_I = \sum_{l=m}^{n} C_l^I \left.\frac{\partial u}{\partial \eta}\right|_{i+l,j} \tag{17}$$

where

$$\left.\frac{\partial u}{\partial \eta}\right|_{i,j} = \frac{1}{\Delta\eta}\sum_{l=p}^{q} C_l^c u_{i,j+l} \tag{18}$$

By choosing different ranges for $(m,n),(r,s),(p,q)$ and different coefficients C_l^I, D_l^I, C_l^c, one can obtain different order accuracy approximation to the viscous terms. The principle of choosing $(m,n),(r,s),(p,q)$ is to ensure that the approximation of $\frac{\partial R}{\partial \xi}|_i$ in Eq. (10) is a central differencing. For example, in this paper, $(m,n)=(-2,1),(r,s)=(-3,2)$, and $p,q)=(-2,2)$ are used, and they give

$$\mu_I = \sum_{l=m}^{n} C_l^I \mu_{i+l} + O(\Delta\xi^4), \tag{19}$$

$$\left.\frac{\partial u}{\partial \xi}\right|_I = \frac{1}{\Delta\xi}\sum_{l=r}^{s} D_l^I u_{i+l} + O(\Delta\xi^5), \tag{20}$$

$$\left.\frac{\partial u}{\partial \eta}\right|_I = \sum_{l=m}^{n} C_l^I \left.\frac{\partial u}{\partial \eta}\right|_{i+I,j} + O(\Delta\xi^4, \Delta\eta^4), \tag{21}$$

where

$$\left.\frac{\partial u}{\partial \eta}\right|_{i,j} = \frac{1}{\Delta\eta}\sum_{l=p}^{q} C_l^c u_{i,j+l} + O(\Delta\eta^4) \tag{22}$$

the coefficients C_l^I, D_l^I, C_l^c can be obtained by Taylor's series expansion and are given in Tables 1–3. For example,

$$\begin{cases} \mu_{i-3/2} = \frac{1}{16}(5\mu_{i-2} + 15\mu_{i-1} - 5\mu_i + \mu_{i+1}) + O(\Delta\xi^4) \\ \mu_{i-1/2} = \frac{1}{16}(-\mu_{i-2} + 9\mu_{i-1} + 9\mu_i - \mu_{i+1}) + O(\Delta\xi^4) \\ \mu_{i+1/2} = \frac{1}{16}(\mu_{i-2} - 5\mu_{i-1} + 15\mu_i + 5\mu_{i+1}) + O(\Delta\xi^4) \end{cases} \tag{23}$$

$$\begin{cases} \left.\frac{\partial u}{\partial \xi}\right|_{i-3/2} = \frac{1}{\Delta\xi}\left(\frac{71}{1920}u_{i-3} - \frac{141}{128}u_{i-2} + \frac{69}{64}u_{i-1} + \frac{1}{192}u_i - \frac{3}{128}u_{i+1} + \frac{3}{640}u_{i+2}\right) + O(\Delta\xi^5) \\ \left.\frac{\partial u}{\partial \xi}\right|_{i-1/2} = \frac{1}{\Delta\xi}\left(-\frac{3}{640}u_{i-3} + \frac{25}{384}u_{i-2} - \frac{75}{64}u_{i-1} + \frac{75}{64}u_i - \frac{25}{384}u_{i+1} + \frac{3}{640}u_{i+2}\right) + O(\Delta\xi^5) \\ \left.\frac{\partial u}{\partial \xi}\right|_{i+1/2} = \frac{1}{\Delta\xi}\left(-\frac{3}{640}u_{i-3} + \frac{3}{128}u_{i-2} - \frac{1}{192}u_{i-1} - \frac{69}{64}u_i + \frac{141}{128}u_{i+1} - \frac{71}{1920}u_{i+2}\right) + O(\Delta\xi^5) \end{cases} \tag{24}$$

The other terms are determined similarly. If $\widetilde{R}_{i-1/2}$ takes $\widetilde{R}_{i-1/2} = R_{i-1/2}$, and

Table 1
The coefficients of C_l^I.

I	C_{-2}^I	C_{-1}^I	C_0^I	C_1^I
$i-3/2$	5/16	15/16	−5/16	1/16
$i-1/2$	−1/16	9/16	9/16	−1/16
$i+1/2$	1/16	−5/16	15/16	5/16

Table 2
The coefficients of D_l^I .

I	D_{-3}^I	D_{-2}^I	D_{-1}^I	D_0^I	D_1^I	D_2^I
$i-3/2$	71/1920	−141/128	69/64	1/192	−3/128	3/640
$i-1/2$	−3/640	25/384	−75/64	75/64	−25/384	3/640
$i+1/2$	−3/640	3/128	−1/192	−69/64	141/128	−71/1920

Table 3
The coefficients of C_l^c.

C_{-2}^c	C_{-1}^c	C_0^c	C_1^c	C_2^c
1/12	−8/12	0	8/12	−1/12

$$C_{-1}=\frac{1}{2},\quad C_0=\frac{1}{2};\quad D_{-1}=1,\quad D_0=1;\quad C^c_{-1}=-\frac{1}{2},\quad C^c_1=\frac{1}{2} \tag{25}$$

and the other coefficients are zero, then the scheme (10) is the three point stencil 2nd-order scheme.

For comparison, the terms used in Refs. [13,14] by De Rango and Zingg et al. are given as the following,

$$\begin{cases} \mu_{i-3/2}=\frac{1}{16}(-\mu_{i-3}+9\mu_{i-2}+9\mu_{i-1}-\mu_i)+O(\Delta\xi^4)\\ \mu_{i-1/2}=\frac{1}{16}(-\mu_{i-2}+9\mu_{i-1}+9\mu_i-\mu_{i+1})+O(\Delta\xi^4)\\ \mu_{i+1/2}=\frac{1}{16}(-\mu_{i-1}+9\mu_i+9\mu_{i+1}-\mu_{i+2})+O(\Delta\xi^4) \end{cases} \tag{26}$$

$$\begin{cases} \left.\frac{\partial u}{\partial\xi}\right|_{i-3/2}=\frac{1}{24\Delta\xi}(u_{i-3}-27u_{i-2}+27u_{i-1}-u_i)+O(\Delta\xi^4)\\ \left.\frac{\partial u}{\partial\xi}\right|_{i-1/2}=\frac{1}{24\Delta\xi}(u_{i-2}-27u_{i-1}+27u_i-u_{i+1})+O(\Delta\xi^4)\\ \left.\frac{\partial u}{\partial\xi}\right|_{i+1/2}=\frac{1}{24\Delta\xi}(u_{i-1}-27u_i+27u_{i+1}-u_{i+2})+O(\Delta\xi^4) \end{cases} \tag{27}$$

Compare Eqs. (23) and (24), and (26) and (27), it can be seen that μ_I in the present paper has the same accuracy order as that of De Rango and Zingg et al., but has smaller stencil width $(i-2,\ldots,i+1)$, $\frac{\partial u}{\partial\xi}|_I$ has the same stencil width, but obtains one accuracy order higher than that of De Rango and Zingg et al. in Refs. [13,14].

It can be proved below that Eq. (10) is symmetric with respect to cell i. Let's take a single term from Eq. (10) as the example:

$$\frac{1}{\Delta\xi}\left[\left(\widetilde{\mu\frac{\partial u}{\partial\xi}}\right)_{i+1/2}-\left(\widetilde{\mu\frac{\partial u}{\partial\xi}}\right)_{i-1/2}\right] \tag{28}$$

where

$$\left(\widetilde{\mu\frac{\partial u}{\partial\xi}}\right)_{i-1/2}=\sum_{I=i-3/2}^{i+1/2}\alpha_I\left(\mu\frac{\partial u}{\partial\xi}\right)_I$$

Both $\left(\widetilde{\mu\frac{\partial u}{\partial\xi}}\right)_{i-1/2}$ and $\left(\widetilde{\mu\frac{\partial u}{\partial\xi}}\right)_{i+1/2}$ are evaluated by Eqs. (15)–(18). The coefficients C^I_l and D^I_l in Tables 1 and 2 are based on interface $i-\frac{1}{2}$. For $\left(\widetilde{\mu\frac{\partial u}{\partial\xi}}\right)_{i+1/2}$, the interfaces used are off set by 1. To distinguish the coefficients from those for $\left(\widetilde{\mu\frac{\partial u}{\partial\xi}}\right)_{i-1/2}$, $\widetilde{C}^I_l$, $\widetilde{D}^I_l$ and $\tilde{\alpha}_I$ are used for $\left(\widetilde{\mu\frac{\partial u}{\partial\xi}}\right)_{i+1/2}$. Based on Tables 1 and 2, we have

$$\widetilde{C}^I_l=C^{I-1}_{l-1},\quad \widetilde{D}^I_l=D^{I-1}_{l-1},\quad \tilde{\alpha}_I=\alpha_{I-1},\quad I=i-1/2,i+1/2,i+3/2$$

Substitute Eq. (15)–(18) to Eq. (28), we have

$$\frac{1}{\Delta\xi}\left[\left(\widetilde{\mu\frac{\partial u}{\partial\xi}}\right)_{i+1/2}-\left(\widetilde{\mu\frac{\partial u}{\partial\xi}}\right)_{i-1/2}\right]=\sum_{m=-2}^{1}\sum_{r=-3}^{2}C_{i+m,i+r}\mu_{i+m}u_{i+r} \tag{29}$$

Eq. (29) has totally 24 terms. As the examples, let's examine the coefficients of $\mu_{i-2}u_{i-3}$, $\mu_{i+2}u_{i+3}$, $\mu_{i-1}u_{i-2}$, and $\mu_{i+1}u_{i+2}$, which are the coefficients of the symmetric terms.

$$C_{i-2,i-3}=-\sum_{I=i-3/2}^{i+1/2}\alpha_I C^I_{-2}D^I_{-3}=-\left[\left(\frac{-1}{24}\right)\cdot\frac{5}{16}\cdot\frac{71}{1920}+\frac{26}{24}\cdot\left(\frac{-1}{16}\right)\cdot\left(\frac{-3}{640}\right)+\left(\frac{-1}{24}\right)\cdot\frac{1}{16}\cdot\left(\frac{-3}{640}\right)\right]=\frac{7}{46080}$$

$$C_{i+2,i+3}=\sum_{I=i-1/2}^{i+3/2}\tilde{\alpha}_I\widetilde{C}^I_2\widetilde{D}^I_3=\left(\frac{-1}{24}\right)\cdot\frac{1}{16}\cdot\frac{3}{640}+\frac{26}{24}\cdot\left(\frac{-1}{16}\right)\cdot\frac{3}{640}+\left(\frac{-1}{24}\right)\cdot\frac{5}{16}\cdot\left(\frac{-71}{1920}\right)=\frac{7}{46080}$$

$$\begin{aligned} C_{i-1,i-2}&=\sum_{I=i-1/2}^{i+3/2}\tilde{\alpha}_I\widetilde{C}^I_{-1}\widetilde{D}^I_{-2}-\sum_{I=i-3/2}^{i+1/2}\alpha_I C^I_{-1}D^I_{-2}\\ &=\left(\frac{-1}{24}\right)\cdot\frac{5}{16}\cdot\frac{71}{1920}+\frac{26}{24}\cdot\left(\frac{-1}{16}\right)\cdot\left(\frac{-3}{640}\right)+\left(\frac{-1}{24}\right)\cdot\frac{1}{16}\cdot\left(\frac{-3}{640}\right)\\ &\quad-\left[\left(\frac{-1}{24}\right)\cdot\frac{15}{16}\cdot\left(\frac{-141}{128}\right)+\frac{26}{24}\cdot\frac{9}{16}\cdot\frac{25}{384}+\left(\frac{-1}{24}\right)\cdot\left(\frac{-5}{16}\right)\cdot\frac{3}{128}\right]=-\frac{479}{5760} \end{aligned}$$

$$C_{i+1,i+2} = \sum_{I=i-1/2}^{i+3/2} \tilde{\alpha}_I \tilde{C}_1^I \tilde{D}_2^I - \sum_{I=i-3/2}^{i+1/2} \alpha_I C_1^I D_2^I$$
$$= \left(\frac{-1}{24}\right)\cdot\left(\frac{-5}{16}\right)\cdot\left(\frac{-3}{128}\right) + \frac{26}{24}\cdot\frac{9}{16}\cdot\left(\frac{-25}{384}\right) + \left(\frac{-1}{24}\right)\cdot\frac{15}{16}\cdot\frac{141}{128}$$
$$- \left[\left(\frac{-1}{24}\right)\cdot\frac{1}{16}\cdot\frac{3}{640} + \frac{26}{24}\cdot\left(\frac{-1}{16}\right)\cdot\frac{3}{640} + \left(\frac{-1}{24}\right)\cdot\frac{5}{16}\cdot\left(\frac{-71}{1920}\right)\right] = -\frac{479}{5760}$$

So we have $C_{i-2,i-3} = C_{i+2,i+3}, C_{i-1,i-2} = C_{i+1,i+2}$. Furthermore, it can be proved that the summation of all the coefficients in Eq. (29) is zero. That is,

$$\sum_{m=-2}^{1}\sum_{r=-3}^{2} C_{i+m,i+r} = 0$$

Hence the schemes make Eq. (10) symmetric about grid node i. The symmetry of central differencing for Eq. (10) satisfies the diffusion property of viscous fluxes.

Next, we prove that the 4th-order accuracy given by Eq. (14) is satisfied. Again, take the term $T = \mu\frac{\partial u}{\partial \xi}$ from $\left(\widetilde{\mu\frac{\partial u}{\partial \xi}}\right)_{i-1/2}$ in Eq. (28) as an example, which is located at $I = i - 3/2$. Based on Eqs. (15) and (16), and Taylor's series expansion, there is

$$T^-_{i-3/2} = \left(\sum_{l=m}^{n} C_l^I \mu_{i+l}\right)\left(\frac{1}{\Delta\xi}\sum_{l=r}^{s} D_l^I u_{i+l}\right) = \left[\mu_{i-3/2} + A_I \mu^{(4)}_{i-3/2}\Delta\xi^4 + O(\Delta\xi^5)\right]\left[\left.\frac{\partial u}{\partial \xi}\right|_{i-3/2} + O(\Delta\xi^5)\right]$$
$$= \mu_{i-3/2}\left.\frac{\partial u}{\partial \xi}\right|_{i-3/2} + A_I\mu^{(4)}_{i-3/2}\left.\frac{\partial u}{\partial \xi}\right|_{i-3/2}\Delta\xi^4 + O(\Delta\xi^5) \tag{30}$$

where A_I is the coefficient of Taylor's series expansion, $\mu^{(4)}$ stands for the 4th order derivative of μ. The corresponding symmetric term $T = \mu\frac{\partial u}{\partial \xi}$ from $\left(\mu\frac{\partial u}{\partial \xi}\right)_{i+1/2}$, which is located at $I = i - 1/2$, is

$$T^+_{i-1/2} = \left(\sum_{l=m}^{n} \tilde{C}_l^I \mu_{i+1+l}\right)\left(\frac{1}{\Delta\xi}\sum_{l=r}^{s} \tilde{D}_l^I u_{i+1+l}\right) = \left[\mu_{i-1/2} + \tilde{A}_I \mu^{(4)}_{i-1/2}\Delta\xi^4 + O(\Delta\xi^5)\right]\left[\left.\frac{\partial u}{\partial \xi}\right|_{i-1/2} + O(\Delta\xi^5)\right]$$
$$= \mu_{i-1/2}\left.\frac{\partial u}{\partial \xi}\right|_{i-1/2} + \tilde{A}_I\mu^{(4)}_{i-1/2}\left.\frac{\partial u}{\partial \xi}\right|_{i-1/2}\Delta\xi^4 + O(\Delta\xi^5)$$

Note that $A_I = \tilde{A}_I$, and

$$\mu^{(4)}_{i-1/2}\left.\frac{\partial u}{\partial \xi}\right|_{i-1/2} = \mu^{(4)}_{i-3/2}\left.\frac{\partial u}{\partial \xi}\right|_{i-3/2} + O(\Delta\xi)$$

hence

$$T^+_{i-1/2} - T^-_{i-3/2} = \mu_{i-1/2}\left.\frac{\partial u}{\partial \xi}\right|_{i-1/2} - \mu_{i-3/2}\left.\frac{\partial u}{\partial \xi}\right|_{i-3/2} + O(\Delta\xi^5)$$

The other two terms $(i - 1/2, i + 1/2)$ can be analyzed similarly as above, thus Eq. (14)

$$\frac{1}{\Delta\xi}(\tilde{R}_{i+1/2} - \tilde{R}_{i-1/2}) = R'(\xi_i) + O(\Delta\xi^4)$$

is proved, i.e. the constructed schemes are formally 4th-order accuracy. The central differencing order of accuracy given in Eqs. (19)–(21) is also the maximum that can be achieved using the WENO stencil.

2.4. Structural model

For the computation of the vortex-induced oscillating cylinder, which is elastically supported as shown in Fig. 1 so that it oscillates only in the direction aligned with or normal to the incoming flow, the structural dynamic equations that governs the motion of the cylinder are:

$$m\ddot{x} + C_x\dot{x} + K_x x = D_f \tag{31}$$
$$m\ddot{y} + C_y\dot{y} + K_y y = L_f \tag{32}$$

These equations are solved implicitly together with the equations of flow motion in a fully coupled manner. In Eq. (31), $\ddot{x}, \dot{x}$, and x represent the dimensionless horizontal acceleration, velocity and displacement of the moving object, respectively. Similarly, $\ddot{y}, \dot{y}$, and y in Eq. (32) represent the acceleration, velocity and displacement in the vertical direction. The terms m, L_f, and D_f are the mass, lift, and drag per unit span, respectively, C_x and C_y are the damping coefficients in horizontal

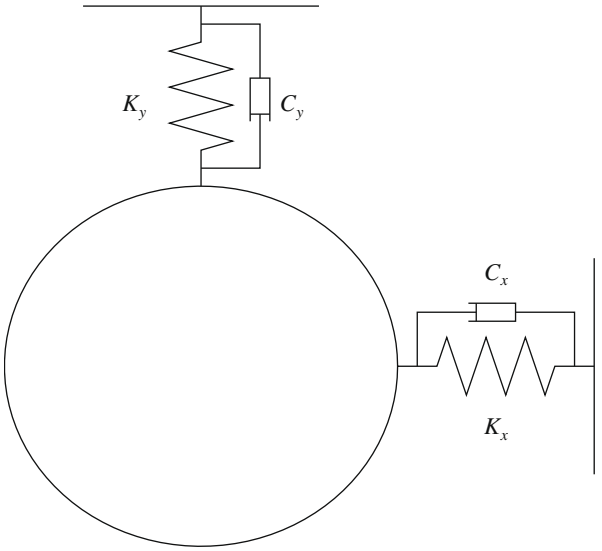

Fig. 1. Sketch of the elastically mounted cylinder.

and vertical directions, and K_x and K_y are the spring constants in horizontal and vertical directions. In the present study, this 'self-excited oscillators' is assumed to have the same response in both directions, i.e. $C_x = C_y$ and $K_x = K_y$.

If the normalization procedure is applied to Eqs. (31) and (32) by using the same reference scales of those used for the equations of flow motion, the following nondimensional equations are obtained:

$$\ddot{x} + 2\zeta\left(\frac{2}{\bar{u}}\right)\dot{x} + \left(\frac{2}{\bar{u}}\right)^2 x = \frac{2}{\mu_s \pi} C_d \tag{33}$$

$$\ddot{y} + 2\zeta\left(\frac{2}{\bar{u}}\right)\dot{y} + \left(\frac{2}{\bar{u}}\right)^2 y = \frac{2}{\mu_s \pi} C_l \tag{34}$$

where ζ is the nondimensional structural damping coefficient calculated by $\zeta = C_{x,y}/\left[2\sqrt{mK_{x,y}}\right]$, $\bar{u}$ is the reduced velocity defined by $\bar{u} = U_\infty/b\omega$,$b$ is radius of the cylinder, $\omega = \sqrt{K_{x,y}/m}$, the mass ratio defined by $\mu_s = m/\pi\rho_\infty b^2$, and C_d and C_l are the drag and lift coefficients, respectively. Then the equations are transformed to a state form and expressed by:

$$[\mathbf{M}]\frac{\partial\{\mathbf{S}\}}{\partial t} + [\mathbf{K}]\{\mathbf{S}\} = \mathbf{q} \tag{35}$$

where

$$\mathbf{S} = \begin{pmatrix} x \\ \dot{x} \\ y \\ \dot{y} \end{pmatrix}, \quad \mathbf{M} = [I], \quad \mathbf{K} = \begin{pmatrix} 0 & -1 & 0 & 0 \\ \left(\frac{2}{\bar{u}}\right)^2 & 2\zeta\left(\frac{2}{\bar{u}}\right) & 0 & 0 \\ 0 & 0 & 0 & -1 \\ 0 & 0 & \left(\frac{2}{\bar{u}}\right)^2 & 2\zeta\left(\frac{2}{\bar{u}}\right) \end{pmatrix}, \quad \mathbf{q} = \begin{pmatrix} 0 \\ \frac{2}{\mu_s\pi} C_d \\ 0 \\ \frac{2}{\mu_s\pi} C_l \end{pmatrix}$$

.

2.5. The time discretization [38,39]

A pseudo temporal term $\frac{\partial Q}{\partial \tau}$ is added to the governing Eq. (5) for the unsteady calculation. The physical temporal term $\frac{\partial Q}{\partial t}$ is discretized implicitly using a 2nd-order three point, backward differencing as the following

$$\frac{\partial Q}{\partial t} = \frac{3Q^{n+1} - 4Q^n + Q^{n-1}}{2\Delta t}$$

and the pseudo temporal term is discretized with first order Euler scheme to enhance diagonal dominance. The semi-discretized governing Eq. (5) can then be expressed as

$$\left[\left(\frac{1}{\Delta\tau} + \frac{1.5}{\Delta t}\right)I - \left(\frac{\partial R}{\partial Q}\right)^{n+1,m}\right]\delta Q^{n+1,m+1} = R^{n+1,m} - \frac{3Q^{n+1,m} - 4Q^n + Q^{n-1}}{2\Delta t} \tag{36}$$

where n is the physical time level index, m is the iteration index within a physical time step, Δt and $\Delta\tau$ are the physical and pseudo time step, R is the net flux evaluated on a grid point, respectively. Eq. (36) is solved using the unfactored Gauss–Seidel line iteration [38,45,46].

To couple the structural equations with the equations of flow motion and solve them implicitly in each physical time step, Eq. (35) is discretized and integrated in a manner consistent with Eq. (36)

$$\left(\frac{1}{\Delta\tau}\mathbf{I}+\frac{1.5}{\Delta t}\mathbf{M}+\mathbf{K}\right)\delta S^{n+1,m+1}=-\mathbf{M}\frac{3\mathbf{S}^{n+1,m}-4\mathbf{S}^{n}+\mathbf{S}^{n-1}}{2\Delta t}-\mathbf{K}\mathbf{S}^{n+1,m}+\mathbf{q}^{n+1,m+1} \tag{37}$$

where n is the physical time level index and m stands for the pseudo time index.

The detailed coupling procedure between the fluid and structural systems can be referred in Ref. [39]. Within a physical time step, the structural motion and the flow field are unknown and are solved iteratively between the fluid and structural systems in a fully couple manner. In our study, within each physical time step, 80 pseudo time steps are used with the L_2 Norm residual reduced by 8 order of magnitude.

3. Results and discussion

3.1. Comparison of scheme accuracy

This subsection is to compare the accuracy of three different schemes: the three point stencil 2nd-order scheme, the 4th-order scheme suggested in [13,14], and the present 4th-order scheme. In order to match the form of the viscous terms in compressible Navier–Stokes equations, the testing function is taken as

$$\frac{\partial}{\partial x}\left(\mu\frac{\partial f}{\partial x}\right)$$

and two cases are validated:

(1)

$$\mu=Ae^{-2x},\quad f(x)=\frac{1-e^{-Rx}}{1-e^{-R}},\quad 0\leqslant x\leqslant 1$$

and $A=0.01,\ R=20$. The function $f(x)$ has the similar distribution as the velocity of a wall boundary layer.

(2)

$$\mu=Ae^{2x},\quad f(x)=sin(Bx),\quad 0\leqslant x\leqslant 1$$

and $A=0.1, B=10$. This function $f(x)$ represents a high frequency wave.

Tables 4 and 5 give the accuracy comparison. It can be seen that the three schemes achieve the expected accuracy. For the two 4th-order schemes, although both of them are fourth order accuracy, the absolute errors of the present scheme are smaller and are about half of those generated by the schemes suggested by De Rango and Zingg et al. [13,14].

For calculating of the function $\frac{\partial}{\partial x}(\mu\frac{\partial f}{\partial x})$, the CPU time used by the 4th-order scheme given in [13,14] and the present 4th-order scheme are 1.40 and 3.45 times of that of the 2nd-order scheme, respectively. However, for solving Navier–Stokes

Table 4
Accuracy comparison of case (1).

Scheme	N	L_∞ error	L_∞ order	L_1 error	L_1 order
2nd	20	0.4264	–	3.1956e−2	–
	40	0.1036	2.041	6.1242e−3	2.383
	80	2.5727e−2	2.010	1.3376e−3	2.195
	160	6.4204e−3	2.003	3.1236e−4	2.098
	320	1.6044e−3	2.001	7.5463e−5	2.049
4th ([14])	20	5.4198e−2	–	4.0620e−3	–
	40	3.2301e−3	4.069	1.9088e−4	4.411
	80	1.9939e−4	4.018	1.0367e−5	4.203
	160	1.2423e−5	4.005	6.0440e−7	4.100
	320	7.7584e−7	4.001	3.6492e−8	4.050
4th (present)	20	2.7556e−2	–	2.0653e-3	–
	40	1.8554e−3	3.893	1.0964e−4	4.236
	80	1.1753e−4	3.981	6.1103e−6	4.165
	160	7.3680e−6	3.996	3.5846e−7	4.091
	320	4.6085e−7	3.999	2.1676e−8	4.048

Table 5
Accuracy comparison of case (2).

Scheme	N	L_∞ error	L_∞ order	L_1 error	L_1 order
2nd	20	1.0566	–	0.3859	–
	40	0.2657	1.992	9.6471e−2	2.000
	80	6.6527e−2	1.998	2.4151e−2	1.998
	160	1.6644e−2	1.999	6.0415e−3	1.999
	320	4.1628e−3	2.000	1.5113e−3	1.999
4th ([14])	20	3.1101e−2	–	1.1432e−2	–
	40	1.9798e−3	3.974	7.2257e−4	3.984
	80	1.2455e−4	3.991	4.5257e−5	3.997
	160	7.7905e−6	3.999	2.8311e−6	3.999
	320	4.8722e−7	3.999	1.7695e−7	4.000
4th (present)	20	1.9647e−2	–	6.8659e−3	–
	40	1.2169e−3	4.013	4.2900e−4	4.000
	80	7.5868e−5	4.004	2.6950e−5	3.993
	160	4.7388e−6	4.001	1.6895e−6	3.996
	320	2.9628e−7	3.999	1.0575e−7	3.998

equations, the CPU time increase of the two 4th-order schemes is only a few percent since the other operation of the Navier–Stokes solver is dominant. This can be seen in the next section.

3.2. Wall boundary layer

A steady state laminar supersonic boundary layer flow on an adiabatic flat plate is employed to validate the present methodology. The incoming Mach number is 2.0. The Reynolds number based on the length of the flat plate is 4.0×10^4. The Prandtl number of 1.0 is used in order to compare with the analytical solution. The computation domain is taken to be $[0, 2] \times [0, 1.6]$. The mesh size is 180×80, and the*CFL* number of 200 is used.

For the comparison purpose, the viscous terms are discretized by using the three point stencil 2nd-order scheme, the 4th-order scheme given in [13,14] and the present 4th-order scheme, respectively. The velocity and temperature profiles shown in Figs. 2 and 3 indicate that all the numerical results agree excellently with the Blasius solution.

Table 6 gives the convergence and CPU information. The convergence condition is that the maximal residual is smaller than 10^{-13}. All the three schemes use 218 steps to reach the convergence condition. This indicates that the high order discretization of viscous terms almost has no effect on the convergence rate. The comparison of CPU time used shows that the 4th-order scheme of De Rango and Zingg et al. [13,14] is 4.9% more than the 2nd-order scheme, and the present 4th-order scheme is 11.8% more than the 2nd-order scheme.

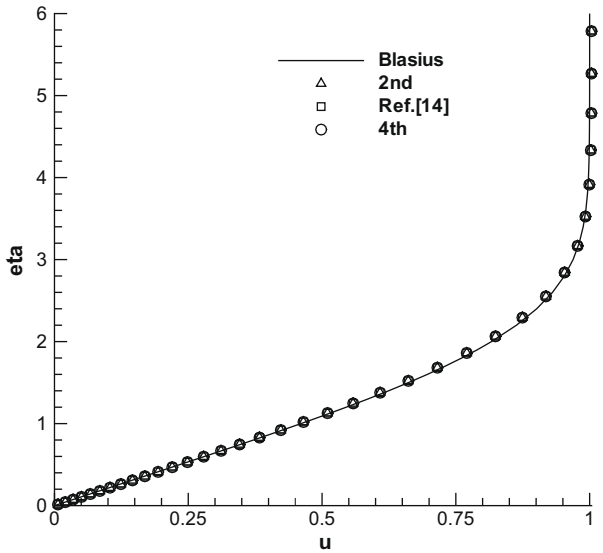

Fig. 2. Comparison of the velocity profiles of the supersonic laminar boundary layer flow.

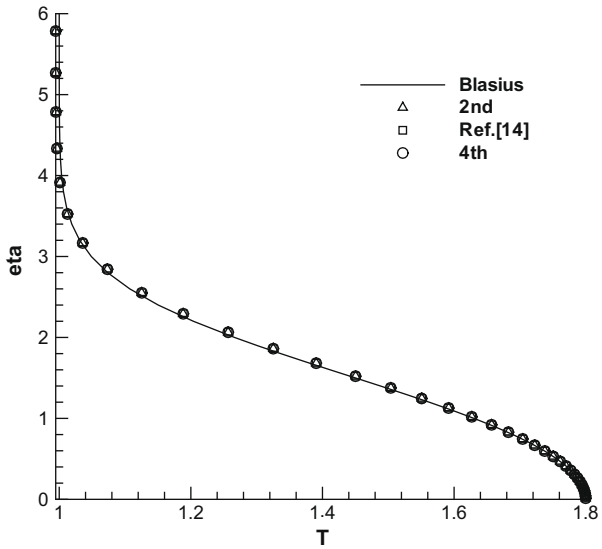

Fig. 3. Comparison of the temperature profiles of the supersonic laminar boundary layer flow.

Table 6
The comparison of different scheme for viscous terms.

Scheme	Steps	CPU time (s)	Percent (%)
2nd	218	62.9	100.0
4th (Ref. [14])	218	66.0	104.9
4th (present)	218	70.3	111.8

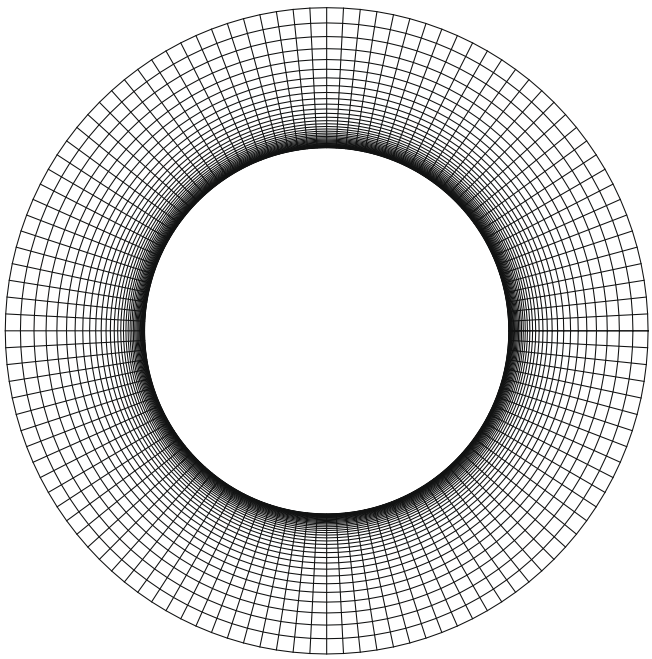

Fig. 4. The near wall zone mesh around the solid surface of the cylinder.

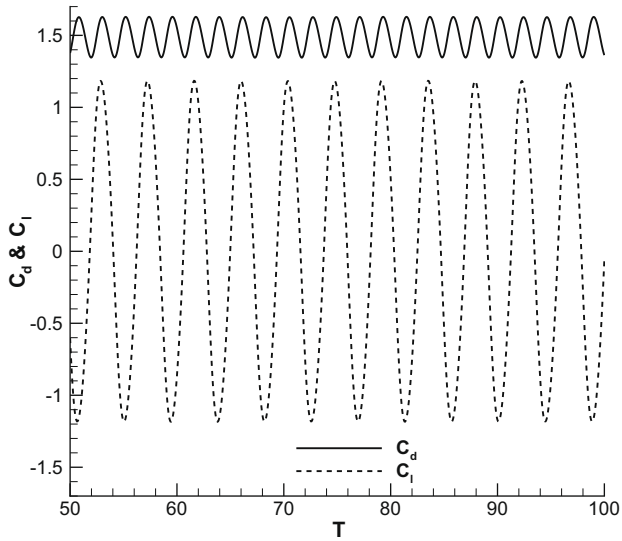

Fig. 5. Time histories of lift and drag coefficients of the stationary cylinder due to vortex shedding.

Table 7
Results of refinement and comparison with the experiments.

Scheme	Mesh dimension	St_{C_d}	St_{C_l}	C_l	C_d
2nd	120×80	0.4497	0.2247	1.188	1.479
	240×160	0.4633	0.2258	1.166	1.480
4th (Ref. [14])	120×80	0.4494	0.2247	1.186	1.477
	240×160	0.4513	0.2258	1.165	1.479
4th (present)	120×80	0.4497	0.2248	1.186	1.477
	240×160	0.4517	0.2258	1.165	1.480
Ref. [39]	120×80	0.4395	0.2197	1.181	1.453
	200×120	0.4516	0.2246	1.227	1.484
Ref. [49]	384×96	0.4674	0.2331	1.149	1.315
Ref. [47]			0.2075		
Ref. [48]			0.2066		

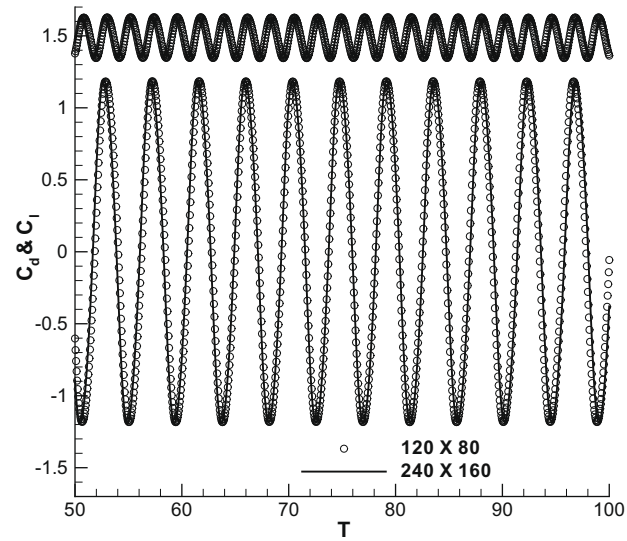

Fig. 6. Comparison of the baseline and refined mesh results for the stationary cylinder.

3.3. Stationary cylinder

The flow past a stationary cylinder is used as the unsteady flow validation case. The zoomed mesh near the cylinder is shown in Fig. 4. The baseline mesh dimensions are 120×80 in circumferential and radial directions. After intensive numerical experiments, the far field boundary is chosen to be located 20 diameters away from the center of the cylinder because the solution is not sensitive to the far field boundary at this range. The Reynolds number based on the free-stream condition and cylinder diameter is $\mathrm{Re} = 500$.

The computed drag and lift coefficients are shown in Fig. 5. As shown in the figure, the lift oscillates at a certain frequency in terms of the Strouhal number St_{C_l}. The drag coefficient oscillates with twice that frequency, St_{C_d}. Table 7 shows that the results are in good agreement with the experiment [47,48] and the results of other researchers [39,49]. There is only a slight difference among three different viscous schemes.

Fig. 6 shows the comparison of the results with refined mesh 240×160. There is little difference between the results of the baseline mesh and refined mesh. This shows that the mesh system 120×80 is sufficient for this problem with $\mathrm{Re} = 500$.

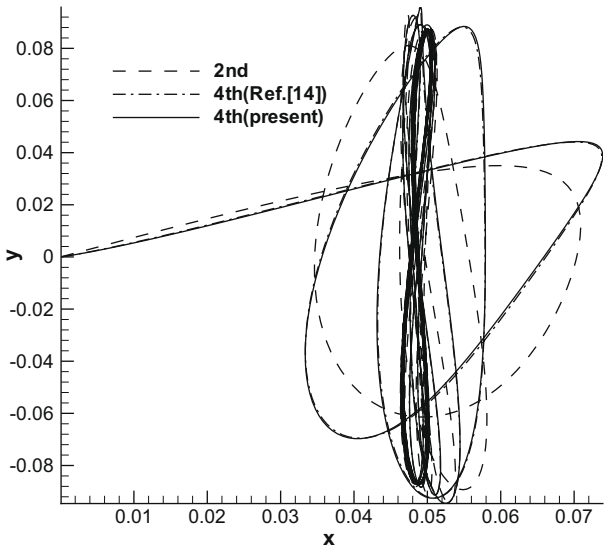

Fig. 7. Comparison of the trajectories using different schemes, $\mu_s = 12.7324, \bar{u} = 1.5915, \zeta = 0.1583$.

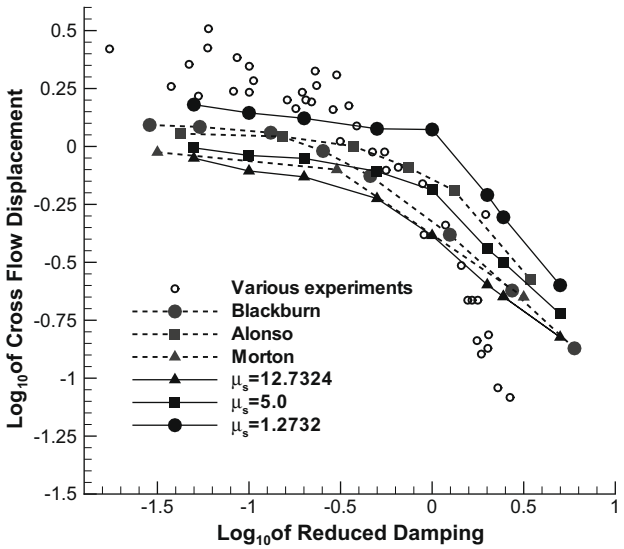

Fig. 8. Comparison of the computed amplitude with Griffin's experiment for the elastically mounted cylinder.

3.4. Vortex-induced vibration of circular cylinder

After the stationary cylinder vortex shedding flow becomes dynamically stable, the cylinder is released to be controlled by the structure model as shown in Fig. 1. Same as the stationary cylinder case, a low Reynolds number, Re = 500, is used. For the purpose of comparison with the experimental data of [50], several different combinations of structural parameters are used in the computation.

In this study, for all the cases of oscillating cylinder, Strouhal number is set to be 0.2, corresponding to $\bar{u} = 1.5915$. Different mass ratios, μ_s, are used to test the different responses of the structural system. They are equal to 1.2732, 5.0, and 12.7324, respectively. To match the wide range of the experimental data, the damping ratio, ζ, is varied in the range 0.001–1.583.

First, the comparison for three different viscous scheme is given for the case of $\mu_s = 12.7324$, $\bar{u} = 1.5915$, $\zeta = 0.1583$. Fig. 7 is the trajectories. It can be seen that, although almost the same final trajectories are obtained by different schemes, the paths approaching the final trajectories are quite different for 4th-order scheme and 2nd-order scheme. The displace-

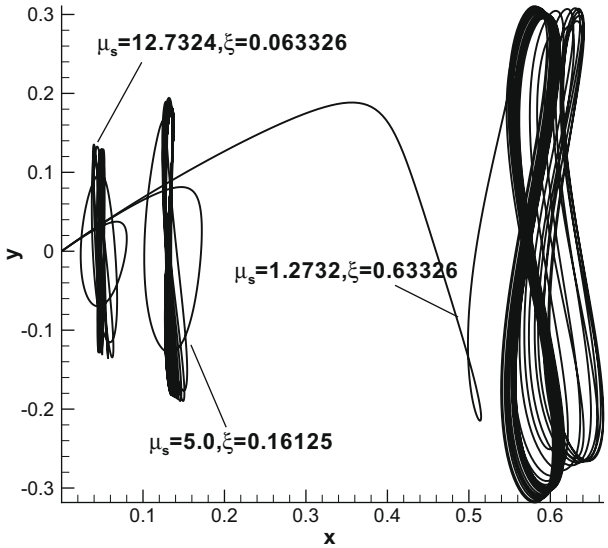

Fig. 9. Comparison of the trajectories at reduced damping coefficient of 2.0.

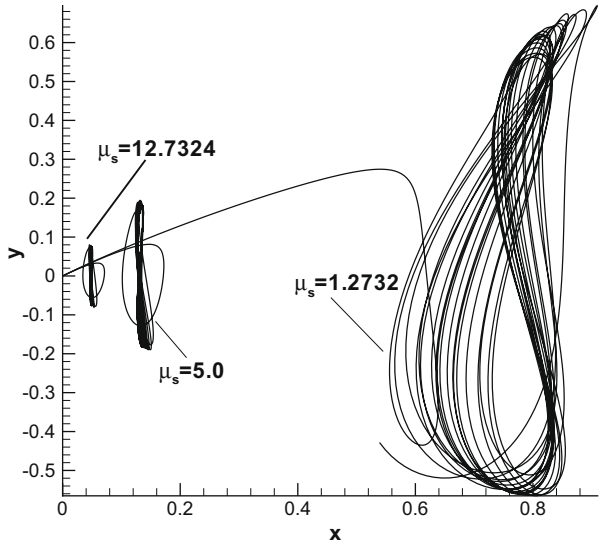

Fig. 10. Comparison of the trajectories with $\zeta = 0.1583$.

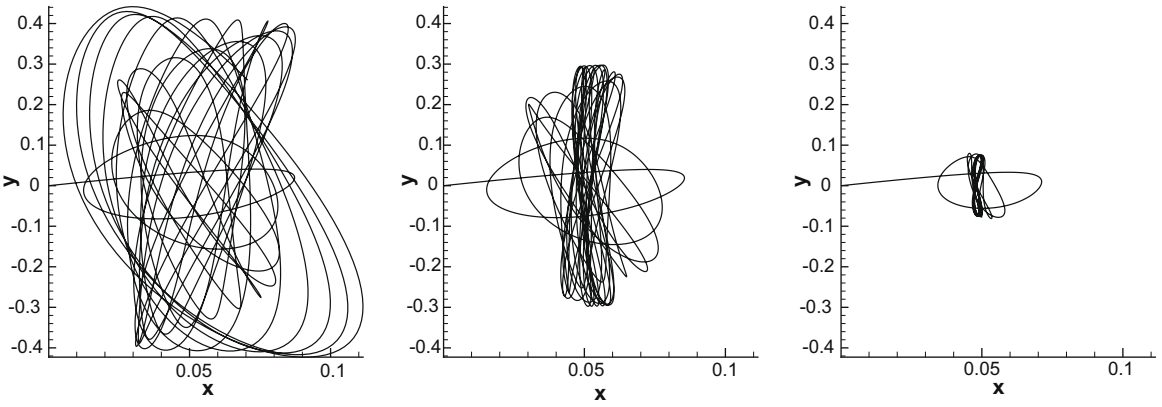

Fig. 11. Comparison of the trajectories with $\mu_s = 12.7324$, from left to right, $\zeta = 0.001583$, $\zeta = 0.01583$, and $\zeta = 0.1583$.

ments in y-direction calculated by the 2nd-order, the 4th-order of De Rango and Zingg et al. [13,14] and the present 4th-order schemes are somewhat different and are 0.1743, 0.1733, and 0.1731, respectively. The two 4th-order schemes are in good agreement.

The numerical results for present study are plotted in Fig. 8 for the three values of μ_s. Also plotted are the computations conducted in [49] with $\mu_s = 5.0$, computations in [51] with $\mu_s = 12.73$, and the experimental data given in [50]. In Fig. 8, the abscissa is the reduced damping coefficient with the form of $8\pi^2 St^2 \zeta m/\rho D^2$ [52], and the ordinate is the cross-flow displacement of motion normalized by the diameter of the cylinder. Overall, a good agreement is observed between the present results and the experimental results. The low damping ratio case with $\mu_s = 1.2732$ shows better agreement with the experiments. The results of $\mu_s = 5.0$ and $\mu_s = 12.7324$ are consistent with the numerical results conducted by other researchers.

Figs. 9–11 are the comparison of the trajectories at different conditions. At the reduced damping coefficient of 2.0, Fig. 9 shows that the trajectories are similar to the results computed in [52] and [49]. With the same $\zeta = 0.1583$, Fig. 10 shows that decreased μ_s results in the trajectory more asymmetrical. From Fig. 11, it can be seen that, for the same $\mu_s = 12.7324$, the trajectory of $\zeta = 0.001583$ is quite irregular due to the smaller damping constrain. When ζ is increased, the amplitude of vibration is decreased.

4. Conclusion

A set of conservative 4th-order central differencing schemes for the viscous terms of compressible Navier–Stokes equations are suggested and proved in this paper. These schemes are used with the 5th-order WENO schemes for inviscid flux. The algorithm is used to simulate the vortex-induced oscillations of an elastically mounted circular cylinder.

The conservative 4th-order viscous schemes have the following features:

(1) For the viscous fluxes of compressible Navier–Stokes equations at an interface, all the terms at the associated interfaces are evaluated using the same stencil. The schemes achieve the maximum order of accuracy within the stencil width of the WENO scheme.
(2) The schemes are symmetric central differencing with respect to the grid node. The symmetry satisfies the diffusion property of a viscous flux.
(3) For viscosity coefficient, the stencil width of the present scheme is two points less than the existing scheme of De Rango and Zingg. For the cross derivatives, the treatment of the first direction has the same formulation as that for the viscosity coefficient. Hence the stencil width in the first direction is also two points less. The narrower stencil is very useful to facilitate boundary condition treatment.

The schemes are validated with the flow of supersonic flat plate boundary layer flow and the flow past a stationary cylinder. Excellent agreement with theoretical results and experiments are obtained.

The algorithm is then applied to simulate the vortex-induced vibration of a circular cylinder. The variation of lift coefficient, drag coefficient, and trajectory under different conditions are investigated. If the reduced damping or the structural damping coefficient is fixed, the larger the mass ratio, the smaller the amplitude. With the increased mass ratio, the amplitude of lift increases slightly, but the drag amplitude increases significantly. If a mass ratio is specified, the smaller damping coefficient induces more irregular trajectory. The increased damping coefficient leads to lift increase and drag decrease. The computed cylinder vibration displacement is in good agreement with experiment.

Acknowledgments

This work is supported by AFOSR Grant FA9550-06-1-0198 monitored by Dr. Fariba Fahroo and supported by Miami Wind™ at University of Miami.

References

[1] J.A. Ekaterinaris, High-order accurate low numerical diffusion methods for aerodynamics, Progress in Aerospace Sciences 41 (2005) 192–300.
[2] Z.J. Wang, High-order methods for the Euler and Navier–Stokes equations on unstructured grids, Progress in Aerospace Sciences 43 (2007) 1–41.
[3] A. Harten, B. Engquist, S. Osher, S. Chakravarthy, Uniformly high order essentially non-oscillatory schemes, III, Journal of Computational Physics 71 (1987) 231–303.
[4] C.-W. Shu, O. Osher, Efficient implementation of essentially non-oscillatory shock capturing schemes, Journal of Computational Physics 77 (1988) 439–471.
[5] G.S. Jiang, C.W. Shu, Efficient implementation of weighted ENO schemes, Journal of Computational Physics 126 (1996) 202–228.
[6] C.W. Shu, Essentially non-oscillatory and weighted essentially non-oscillatory schemes for hyperbolic conservation laws, NASA/CR-97-206253, ICASE Report No. 97-65, Nov. 1997.
[7] D.S. Balsara, C.-W. Shu, Monotonicity preserving weighted essentially non-oscillatory schemes with increasingly high order of accuracy, Journal of Computational Physics 160 (2000) 405–452.
[8] Y.Q. Shen, G.-C. Zha, Improvement of the WENO scheme smoothness estimator, AIAA Paper 2008-3993, June 2008.
[9] Y.-Q. Shen, G.-C. Zha, B.-Y. Wang, Improvement of stability and accuracy of implicit WENO scheme, AIAA Journal 47 (2009) 331–344.
[10] V.A. Titarev, E.F. Toro, Finite-volume WENO schemes for three-dimensional conservation laws, Journal of Computational Physics 201 (2004) 238–260.
[11] T. Zhou, Y. Li, C.W. Shu, Numerical comparison of WENO finite volume and Runge–Kutta discontinuous Galerkin methods, Journal Scientific Computing 16 (2001) 145–171.
[12] S.A. Lele, Compact finite difference schemes with spectral-like resolution, Journal of Computational Physics 103 (11) (1992) 6–42.
[13] S. De Rango, D.W. Zingg, Aerodynamic computations using a higher-order algorithm, AIAA 99-0167, 1999.
[14] D.W. Zingg, S. De Rango, M. Nemec, T.H. Pulliam, Comparison of several spatial discretizations for the Navier–Stokes equations, Journal of Computational Physics 160 (2000) 683–704.
[15] Y.Q. Shen, B.Y. Wang, G.C. Zha, Implicit WENO scheme and high order viscous formulas for compressible flows, AIAA-2007-4431, June 2007.
[16] T. Sarpkaya, A critical review of the intrinsic nature of vortex-induced vibrations, Journal of Fluids and Structures 19 (2004) 389–447.
[17] C.H.K. Williamson, R. Govardhan, Vortex-induced vibrations, Annual Review of Fluid Mechanics 36 (2004) 413–455.
[18] C.H.K. Williamson, R. Govardhan, A brief review of recent results in vortex-induced vibrations, Journal of Wind Engineering and Industrial Aerodynamics (2007), doi:10.1016/j.jweia.2007.06.019.
[19] H. Al Jamal, C. Dalton, The contrast in phase angles between forced and self-excited oscillations of a circular cylinder, Journal of Fluids and Structures 20 (2005) 467–482.
[20] R.D. Gabbai, H. Benaroya, An overview of modeling and experiments of vortex-induced vibration of circular cylinders, Journal of Sound and Vibrations 282 (2005) 575–616.
[21] S. Meynen, H. Verma, P. Hagedorn, M. Schafer, On the numerical simulation of vortex-induced vibrations of oscillating conductors, Journal of Fluids and Structures 21 (2005) 41–48.
[22] S. Mittal, A. Raghuvanshi, Control of vortex shedding behind circular cylinder for flows at low Reynolds numbers, International Journal for Numerical Methods in Fluids 35 (2001) 421–447.
[23] S. Mittal, V. Kumar, Flow-induced vibrations of a light circular cylinder at Reynolds numbers 10^3–10^4, Journal of Sound and Vibration 245 (2001) 923–946.
[24] T.K. Prasanth, S. Behara, S.P. Singh, R. Kumar, S. Mittal, Effect of blockage on vortex-induced vibrations at low Reynolds numbers, Journal of Fluids and Structures 22 (2006) 865–876.
[25] H.M. Blackburn, R.D. Henderson, A study of the two-dimensional flow past an oscillating cylinder, Journal of Fluid Mechanics 385 (1999) 255–286.
[26] H.M. Blackburn, R.N. Govardhan, C.H.K. Williamson, A complementary numerical and physical investigation of vortex-induced, Journal of Fluids and Structures 15 (2000) 481–488.
[27] C. Evangelinos, D. Lucor, G.E. Karniadakis, DNS-derived force distribution on flexible cylinders subject to vortex-induced vibration, Journal of Fluids and Structures 14 (2000) 429–440.
[28] D. Lucor, J. Foo, G.E. Karniadakis, Vortex mode selection of a rigid cylinder subject to VIV at low mass-damping, Journal of Fluids and Structures 20 (2005) 483–503.
[29] S. Dong, G.E. Karniadakis, DNS of flow past a stationary and oscillating cylinder at Re = 10,000, Journal of Fluids and Structures 20 (2005) 519–531.
[30] J.B.V. Wanderley, C.A. Levi, Validation of a finite difference method for the simulation of vortex-induced vibrations on a circular cylinder, Ocean Engineering 29 (2002) 445–460.
[31] K. Ryan, C.J. Pregnalato, M.C. Thompson, K. Hourigan, Flow-induced vibrations of a tethered circular cylinder, Journal of Fluids and Structures 19 (2004) 1085–1102.
[32] A. Placzek, J.F. Sigrist, A. Hamdouni, Numerical simulation of an oscillating cylinder in a cross-flow at low Reynolds number: forced and free oscillations, Computers and Fluids (2008), doi:10.1016/j.compfluid.2008.01.007.
[33] E. Guilmineau, P. Queutey, Numerical simulation of vortex-induced vibration of a circular cylinder with low mass damping, Journal of Fluids and Structures 19 (2004) 449–466.
[34] E. Guilmineau, P. Queutey, A numerical simulation of vortex shedding from an oscillating circular cylinder, Journal of Fluids and Structures 16 (2002) 773–794.
[35] Z.Y. Pan, W.C. Cui, Q.M. Miao, Numerical simulation of vortex-induced vibration of a circular cylinder at low mass-damping using RANS code, Journal of Fluids and Structures 23 (2007) 23–37.
[36] M. Tutar, A.E. Holdo, Large Eddy Simulation of a smooth circular cylinder oscillating normal to a uniform flow, ASME Journal of Fluids Engineering 122 (2000) 694–702.
[37] H. Al Jamal, C. Dalton, Vortex-induced vibrations using large eddy simulation at a moderate Reynolds number, Journal of Fluids and Structures 19 (2004) 73–92.
[38] X.-Y. Chen, G.-C. Zha, Z.-J. Hu, Numerical Simulation of flow induced vibration based on fully coupled–structural interactions, AIAA Paper 2004-2240, AIAA 34th AIAA Fluid Dynamics Conference, 2004.
[39] X. Chen, G.-C. Zha, Fully coupled fluid–structural interactions using an efficient high solution upwind scheme, Journal of Fluid and Structure 20 (2005) 1105–1125.
[40] P. Thomas, C. Lombard, Geometric conservation law and its application to flow computations on moving grids, AIAA Journal 17 (10) (1979) 1030–1037.
[41] D.J. Mavriplis, Z. Yang, Construction of the discrete geometric conservation law for high-order time-accurate simulations on dynamic meshes, Journal of Computational Physics 213 (2006) 557–573.
[42] M.R. Visbal, D.V. Gaitonde, On the use of higher-order finite-difference schemes on curvilinear and deforming meshes, Journal of Computational Physics 181 (2002) 155–185.

[43] R. Kamakoti, W. Shyy, Fluid–structure interaction for aeroelastic applications, Progress in Aerospace Sciences 40 (2004) 535–558.
[44] S. Etienne, A. Garon, D. Pelletier, Perspective on the geometric conservation law and finite element methods for ale simulations of incompressible flow, Journal of Computational Physics 228 (2009) 2313–2333.
[45] Z.-J. Hu, G.-C. Zha, Numerical study on flow separation of a transonic cascade, AIAA Paper 2004-0199, Jan. 2004.
[46] Y.Q. Shen, B.Y. Wang, G.C. Zha, Comparison study of implicit Gauss–Seidel line iteration method for transonic flows, AIAA-2007-4332, June 2007.
[47] A. Roshko, On the development of turbulent wakes from vortex streets, NACA Rep. 1191, 1954.
[48] S. Goldstein, Modern Developments in Fluid Dynamics, Clarendon Press, Oxford, 1938.
[49] J. Alonso, L. Martinelli, A. Jameson, Multigrid unsteady Navier–Stokes calculations with aeroelastic applications, AIAA Paper 95-0048, 1995.
[50] O.M. Griffin, Vortex-induced vibrations of marine structures in uniform and sheared currents, NSF Workshopon Riser Dynamics, University of Michigan, 1992.
[51] S.A. Morton, R.B. Melville, M.R. Visbal, Accuracy and coupling issues of aeroelastic Navier–Stokes solutions on deforming meshes, AIAA Paper-97-1085, 1997.
[52] H. Blackburn, G. Karniadakis, Two and three-dimensional vortex-induced vibration of a circular cylinder, in: ISOPE-93 Conference, Singapore, 1993.